

Characteristic quantities of pion-emitting sources extracted by model-independent analysis in relativistic heavy ion collisions

Wei-Ning Zhang^{1,2*}, Zhi-Tao Yang², and Yan-Yu Ren²

¹*School of Physics and Optoelectronic Technology,
Dalian University of Technology,*

Dalian, Liaoning 116024, P. R. China

²*Department of Physics,
Harbin Institute of Technology, Harbin,
Heilongjiang 150006, P. R. China*

We examine the characteristic quantities of pion-emitting sources extracted by model-independent imaging analysis in relativistic heavy ion collisions. The moments of the spatial separation of pion pair emission can provide the characteristic information about the source geometry and coherence. They are better for describing the non-Gaussian sources with granular and core-halo structures. An improved granular source model of quark-gluon plasma droplets can reproduce the main characteristics of the two-pion correlation functions and source functions in the experiment of $\sqrt{s_{NN}} = 200$ GeV Au+Au collisions. The transverse-momentum dependence of the normalized first-order moments of the separation for the granular source is consistent with that of the usual interferometry results of source radii, after taking into account the Lorentz contraction in the direction of transverse momentum of pion pair.

PACS numbers: 25.75.-q, 25.75.Gz

I. INTRODUCTION

Hanbury-Brown-Twiss (HBT) interferometry has been extensively used to extract the space-time and coherence information about the particle-emitting sources produced in relativistic heavy ion collisions [1, 2, 3, 4]. In conventional two-pion HBT analysis one needs fitting the measured correlation functions with parameterized formulae, e.g., a Gaussian form, to obtain quantitatively the source radii and chaotic parameter. So these quantitative HBT results are model depended. Recently, many studies indicate that the particle-emitting sources produced in relativistic heavy ion collisions are far from Gaussian distributed [5, 6, 7, 8, 9, 10, 11, 12, 13, 14, 15, 16, 17]. For the non-Gaussian sources the conventional HBT method of the Gaussian fit is inappropriate [15, 18, 19, 20, 21]. Therefore, it is important to investigate the source characteristic quantities by model-independent analysis.

The imaging technique introduced by Brown and Danielewicz [5, 22, 23] is a model-independent way to obtain the two-pion source function $S(r)$, the probability for emitting a pion pair with spatial separation r in the pair center-of-mass system (PCMS), from the measured two-pion correlations. This technique has been developed and used in analyzing one- and multi-dimension source geometry in relativistic heavy ion collisions [5, 6, 7, 8, 9, 10, 11, 12, 24, 25, 26, 27, 28, 29, 30, 31]. Recent imaging analyses for the pion-emitting sources produced in relativistic heavy ion collisions suggest that the sources may have a core-halo [6, 7] or granular struc-

ture [12]. In this paper we will examine the characteristic quantities extracted by the imaging analysis for the non-Gaussian sources with granular and core-halo structures. We find that the zero-order moment of r , corresponding to the intercept of the two-pion correlation function at zero relative momentum, is usually larger than the chaotic parameter obtained by the HBT Gaussian fit. The first-order moment and standard deviation of r , which are normalized to the Gaussian radius for a Gaussian source, can be used to characterize the source size and the deviation of the source distribution from Gaussian form.

In Ref. [16], a granular source model was used to explain the HBT puzzle, $R_{out}/R_{side} \sim 1$, in the Relativistic Heavy Ion Collider (RHIC) experiments [32, 33, 34, 35]. Here R_{out} and R_{side} are the HBT radii in the directions parallel and perpendicular to the transverse momentum of pion pair [36, 37]. However, in the previous granular source models [16, 38], all the droplets are assumed with the same initial radius and pions are emitted at a fixed freeze-out temperature T_f . In this paper we will improve the granular source model by introducing random initial radii of the droplets according to a Gaussian distribution and letting the pions emit in a wide T_f region for including both directly produced and decayed pions. We will investigate the characteristic quantities extracted by the three-dimension imaging analysis [30, 31] for the improved granular source. We find that the improved granular source mode can reproduce the main characteristics of the experimental two-pion correlation functions and source functions in $\sqrt{s_{NN}} = 200$ GeV Au+Au collisions [10, 34, 35]. The transverse-momentum dependence of the normalized first-order moments agrees with that of the HBT radii obtained by usual Gaussian fit, after tak-

*wnzhang@dlut.edu.cn

ing into account the Lorentz contraction in the direction of transverse momentum of pion pair.

The paper is organized as follows. In section II, we discuss briefly the limitation of the HBT Gaussian fit for the non-Gaussian sources with granular and core-halo structures. The model-independent characteristic quantities extracted by imaging analysis are examined for the non-Gaussian sources and compared with the HBT results of the Gaussian fit. In section III we introduce an improved granular source model of QGP droplets to simulate the two-pion HBT correlations in relativistic heavy ion collisions. In section IV we investigate the three-dimension source functions for the improved granular source. The transverse-momentum dependence of the characteristic quantities of the source functions are investigated in different directions. Finally, a summary and conclusion is given in section V.

II. GAUSSIAN FIT AND IMAGING ANALYSIS IN HBT INTERFEROMETRY

In this section we discuss the quantitative results extracted by the usual Gaussian fit and a model-independent imaging analysis in HBT interferometry. For a direct comparison with analytical results, we consider in this section only the static sources with spherical symmetry.

A. Gaussian fit

In conventional HBT analysis, the measured two-pion correlation functions are fitted with a Gaussian formula to obtain quantitative results. Using the relative-momentum q of the pair as a variable, the Gaussian fitting formula is

$$C(q) = 1 + \mathcal{R}(q) = 1 + \lambda_{\text{hbt}} \exp(-q^2 R_{\text{hbt}}^2), \quad (1)$$

where R_{hbt} and λ_{hbt} are called the HBT radius and chaotic parameter of the pion-emitting source.

Let us examine the fitting procedure. The chi-square function is [21]

$$\chi^2 \equiv \sum_i \left[\frac{\ln \mathcal{R}_i - \ln \lambda_{\text{hbt}} + q_i^2 R_{\text{hbt}}^2}{\sigma_i'} \right]^2, \quad (2)$$

where \mathcal{R}_i is the i th measured correlator at q_i , $\sigma_i' = \sigma_i / \mathcal{R}_i$, and σ_i is the error of \mathcal{R}_i . Minimizing the χ^2 with respect to the fitting parameters R_{hbt}^2 and $\ln \lambda_{\text{hbt}}$,

$$\frac{\partial \chi^2}{\partial (R_{\text{hbt}}^2)} = 0, \quad \frac{\partial \chi^2}{\partial (\ln \lambda_{\text{hbt}})} = 0, \quad (3)$$

one obtains

$$R_{\text{hbt}}^2 = \frac{\sum_{i,j} a_i a_j (b_i - b_j) q_i^2}{\sum_{i,j} a_i a_j (q_i^2 - q_j^2) q_i^2}, \quad (4)$$

$$\ln \lambda_{\text{hbt}} = - \frac{\sum_{i,j} a_i a_j b_j (q_i^2 - q_j^2) q_i^2}{\sum_{i,j} a_i a_j (q_i^2 - q_j^2) q_i^2}, \quad (5)$$

where the quantities

$$a_i = \mathcal{R}_i^2 / \sigma_i^2, \quad b_i = \ln \mathcal{R}_i. \quad (6)$$

Introduce

$$A = \sum_j a_j, \quad B = \sum_j a_j b_j, \quad (7)$$

$$C = \sum_j a_j b_j q_j, \quad D = \left| \sum_{i,j} a_i a_j (q_i^2 - q_j^2) q_i^2 \right|, \quad (8)$$

equations (4) and (5) can be expressed as

$$R_{\text{hbt}}^2 = \frac{1}{D} \left| \sum_i (A b_i - B) a_i q_i^2 \right|, \quad (9)$$

$$\ln \lambda_{\text{hbt}} = - \frac{1}{D} \left| \sum_i (B q_i^2 - C) a_i q_i^2 \right|. \quad (10)$$

It can be seen that the term for the contribution of the i th measured correlator has a weight factor of $\mathcal{R}_i^2 q_i^2 / \sigma_i^2$. At a smaller q_i , $\mathcal{R}_i \sim 1$ and σ_i is usually larger than that for a larger q_i . So the contributions from the data at the bins near zero q are very small.

Recent imaging analyses in relativistic heavy ion collisions exhibit a two-tiered structure or a long-tail in the two-pion source functions [7, 8, 9, 10, 11, 12]. These non-Gaussian source functions indicate that the pion-emitting sources may have a granular [12] or core-halo [6, 7] structure. Let us examine the Gaussian-fit to the HBT correlation functions of these kinds of non-Gaussian sources.

For the granular source, the pions are assumed to be emitted from separated droplets in the source [12, 16, 38, 39, 40]. Assuming that the distributions of the emitting-points in each droplet and the droplet centers in the source are Gaussian forms with standard deviations a and R_{gr} respectively, the two-pion correlation function for a static granular source is given by [39, 40]

$$C_{\text{gr}}(q) = 1 + \frac{1}{N} e^{-q^2 a^2} + \left(1 - \frac{1}{N}\right) e^{-q^2 (a^2 + R_{\text{gr}}^2)}, \quad (11)$$

where N is the number of droplet in the source. In Eq. (11) the second term is the contribution corresponding to the two pions from the same droplet and the third term is for the pions from different droplets.

For the core-halo source [18, 41], the pions are emitted from a central core and a halo of long-lived resonance decays. Assuming the emitting-points in the core and

halo are all the Gaussian distribution with standard deviations R_c and R_h , the two-pion correlation function of the static core-halo source is given by [18]:

$$C_{\text{ch}}(q) = 1 + f_c^2 e^{-q^2 R_c^2} + (1 - f_c^2) e^{-q^2 R_h^2} + 2f_c(1 - f_c) e^{-q^2 (R_c^2 + R_h^2)/2}, \quad (12)$$

where f_c is the fraction of core emission. The second, third, and fourth terms in Eq. (12) are the contributions for both the two pions from the core, the halo, and one from the core and another from the halo, respectively.

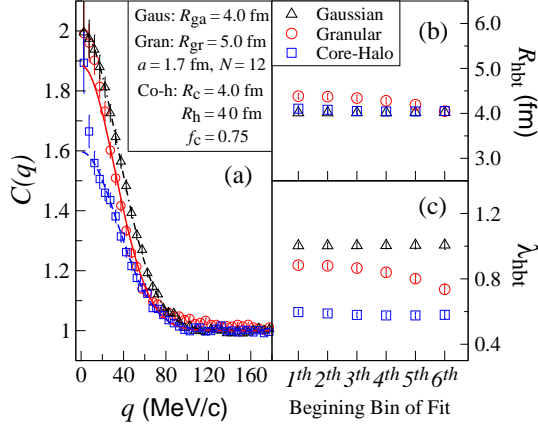


FIG. 1: (Color online) (a) Two-pion correlation functions for completely chaotic Gaussian, granular, and core-halo sources. (b) and (c) The fitted results of R_{hbt} and λ_{hbt} of the Gaussian fit with the data sets beginning from the i th measured correlator.

In Fig. 1(a) we show the simulated two-pion correlations for completely chaotic Gaussian, granular, and core-halo sources, where the lines are the fitted curves of the Gaussian fit, Eq. (1). It can be seen that the fit is very good for the Gaussian source. However, for the granular and core-halo sources the fits are inappropriate, which miss the data of the lower q -bins. In Fig. 1(b) and (c), we exhibit the fitted results of R_{hbt} and λ_{hbt} for the fits which use the data sets beginning from the i th measured correlator. One can see that the fitted results of R_{hbt} are insensitive to the first several data of q -bins. For the core-halo source, the R_{hbt} results are almost the same as that of the Gaussian source. The fitted HBT radii cannot reflect the large spatial extent of the halo for the long-lived resonance decays. Also, because of missing the data of the first one or two q -bins, the results of λ_{hbt} for the core-halo source are about f_c^2 , which is the main reason that a large halo-structure was introduced to explain the low chaotic parameters measured in experiments [18, 41]. For the granular source, the two-tiered structure of the correlations [39, 40] and the failure for the first several data in the Gaussian fit lead to $R_{\text{hbt}} < R_{\text{gr}}$ and $\lambda_{\text{hbt}} < 1$. So, the usual model-dependent HBT fitted results are hardly to reflect the full geometry and coherence of these non-Gaussian sources.

B. Imaging analysis

The imaging technique introduced by Brown and Danielewicz [5, 22, 23] allows one to obtain the two-pion source function $S(r)$ in PCMS, from the measured two-pion correlation function $C(Q)$ ($Q = \sqrt{\mathbf{q}^2 - q_0^2}$). After knowing the source function one can calculate the moments of r model-independently. Define the n th-order moment of r as:

$$\langle r^n \rangle = \frac{4\pi \int_0^\infty dr r^n S(r) r^2}{4\pi \int_0^\infty dr S(r) r^2}, \quad n = 1, 2, \dots, \quad (13)$$

where the denominator is a quantity of normalization as the zero-order moment of r . Denote the zero-order moment of r by $\tilde{\lambda}$,

$$\tilde{\lambda} \equiv 4\pi \int_0^\infty dr S(r) r^2. \quad (14)$$

Theoretically, the value of $\tilde{\lambda}$ is equal to $\mathcal{R}(Q=0)$ [5]. It is unit for a completely chaotic source and between zero and unit for a partially coherent source.

For a completely chaotic Gaussian source, the source function is [5, 23, 25]

$$S_{\text{ga}}(r) = \frac{1}{(\sqrt{4\pi}R_{\text{ga}})^3} \exp\left(-\frac{r^2}{4R_{\text{ga}}^2}\right), \quad (15)$$

where R_{ga} is called as the Gaussian radius of the source. The first- and second-order moments of r for the Gaussian source are:

$$\langle r \rangle_{\text{ga}} = \frac{4}{\sqrt{\pi}} R_{\text{ga}}, \quad \langle r^2 \rangle_{\text{ga}} = 6R_{\text{ga}}^2. \quad (16)$$

The deviation of the Gaussian source function is

$$\sigma = \sqrt{\langle r^2 \rangle - \langle r \rangle^2} = \sqrt{6 - 16/\pi} R_{\text{ga}}. \quad (17)$$

The source functions for completely chaotic granular and core-halo sources are given by [12, 42]

$$S_{\text{gr}}(r) = \frac{1}{N} \frac{1}{(\sqrt{4\pi}a)^3} \exp\left(-\frac{r^2}{4a^2}\right) + \left(1 - \frac{1}{N}\right) \times \frac{1}{[4\pi(a^2 + R_{\text{gr}}^2)]^{3/2}} \exp\left[-\frac{r^2}{4(a^2 + R_{\text{gr}}^2)}\right], \quad (18)$$

$$S_{\text{ch}}(r) = \frac{f_c^2}{(\sqrt{4\pi}R_c)^3} \exp\left(-\frac{r^2}{4R_c^2}\right) + \frac{(1 - f_c)^2}{(\sqrt{4\pi}R_h)^3} \exp\left(-\frac{r^2}{4R_h^2}\right) + \frac{2f_c(1 - f_c)}{[2\pi(R_c^2 + R_h^2)]^{3/2}} \exp\left[-\frac{r^2}{2(R_c^2 + R_h^2)}\right]. \quad (19)$$

In Eq. (18) the first term is the contribution corresponding to the two pions from the same droplet and the second

term is for the two pions from different droplets. In Eq. (19) the first and second terms are the contributions for the two particles both from the core and from the halo, and the third term corresponds to that one particle from the core and another from the halo.

We introduce a normalized first-order moment and a normalized deviation as

$$\tilde{R} \equiv \frac{\sqrt{\pi}}{4} \langle r \rangle \quad (20)$$

and

$$\tilde{\sigma} \equiv \sigma / \sqrt{6 - 16/\pi}. \quad (21)$$

Both the quantities are normalized to the Gaussian radius R_{ga} for a Gaussian source. The normalized moment \tilde{R} describes the source size. It agrees with the HBT radius for a Gaussian source and we shall see that it is greater than the HBT radii for the granular or core-halo source. The normalized deviation $\tilde{\sigma}$ is equal to \tilde{R} for a Gaussian source and larger than \tilde{R} for the granular or core-halo source. One can examine the deviation of source distribution from Gaussian distribution by comparing the values of \tilde{R} and $\tilde{\sigma}$.

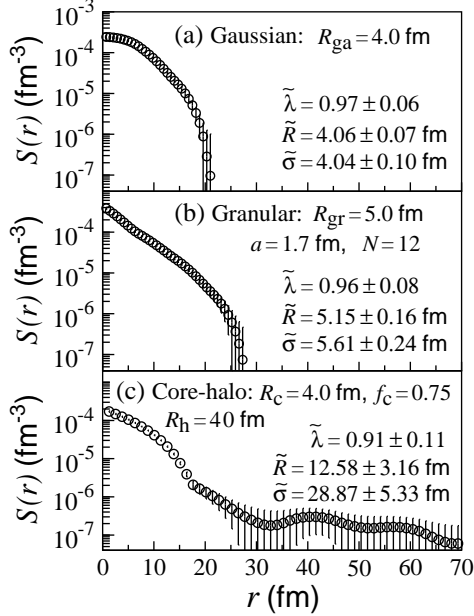


FIG. 2: The two-pion source functions for the Gaussian, granular, and core-halo sources as the same in figure 1.

In Fig. 2 we show the source functions obtained by imaging analysis for the Gaussian, granular, and core-halo sources as in Fig. 1. The values of $\tilde{\lambda}$, \tilde{R} , and $\tilde{\sigma}$ are calculated with the imaging source functions. They are consistent with the corresponding analytical results obtained by Eqs. (15), (18) – (21). It can be seen that the source function of the granular source is wider than that

TABLE I: The characteristic quantities of the granular sources ($R_{\text{gr}} = 5.5 \text{ fm}$).

source parameters	ξ	$\tilde{R} \text{ (fm)}$	$\tilde{\sigma} \text{ (fm)}$
$a = 1.2 \text{ fm}, N = 12$	9.63	5.32 ± 0.13	6.04 ± 0.16
$a = 1.7 \text{ fm}, N = 12$	3.39	5.47 ± 0.12	6.05 ± 0.15
$a = 1.7 \text{ fm}, N = 20$	1.88	5.61 ± 0.13	5.91 ± 0.17

of the Gaussian source. Because of the long-lived resonance halo the source function of the core-halo source has a very long tail. By comparing with the results of the Gaussian fits in Fig. 1, one can see that the results of $\tilde{\lambda}$ and \tilde{R} for the Gaussian source are consistent with the corresponding HBT fitted results of λ_{hbt} and R_{hbt} , respectively. The value of $\tilde{\sigma}$ for the Gaussian source is equal to that of \tilde{R} as expected. For the non-Gaussian sources, the results of $\tilde{\lambda}$ calculated with the source functions are close to unit and give more realistic chaotic degrees of the sources than that given by the λ_{hbt} results. The results of \tilde{R} for the non-Gaussian sources are larger than the corresponding R_{hbt} results. The first-order moment \tilde{R} reflects more about the whole sizes of these non-Gaussian sources than R_{hbt} , because the Gaussian fit is insensitive to the measured data in smaller relative momentum region (corresponding to larger coordinate region). The results of $\tilde{\sigma} > \tilde{R}$ for the non-Gaussian sources reflect the deviations of the source distributions from Gaussian form.

The values of \tilde{R} and $\tilde{\sigma}$ are related to the space-structure of the source. For the granular source the quantity $\xi = [(R_{\text{gr}}/a)^3/(N-2)]$ ($1 < N < R_{\text{gr}}^3/a^3$) characterizes the granularity of the source sensitively [12]. In Table I we list the values of ξ as well as the results of \tilde{R} and $\tilde{\sigma}$ calculated with the imaging source functions for the granular sources with different source parameters. The values of \tilde{R} and $\tilde{\sigma}$ change with the droplet radius a and number N for the sources with the same radius R_{gr} . The difference between the values of \tilde{R} and $\tilde{\sigma}$ increases with ξ . The model-independent observables \tilde{R} and $\tilde{\sigma}$ provide the spatial information of the granular sources.

III. AN IMPROVED GRANULAR SOURCE MODEL

As it is seen in section II, the source functions of the granular and core-halo sources are wider than that of the Gaussian source, which agrees with recent imaging analyses of RHIC experiments [6, 7, 12]. Because granular source model can reproduce the experimental results of HBT radii [16], we construct here an evolution pion-emitting source based on granular source model and take into account the effect of resonance decay by letting pions emit in a wide temperature region.

On the basis of Bjorken picture [43] the systems produced in relativistic heavy ion collisions reach a local-

equilibrium at $\tau_0 \sim 1$ fm/c, then expand hydrodynamically. The expanding velocity of a fluid cell in a central rapidity region $|y| < y_m$ at coordinate point $(r_\perp \equiv \rho, z, t)$ can be expressed as [44]

$$v_\perp = v_\perp(z=0)\sqrt{1-v_z^2}, \quad v_z = z/t. \quad (22)$$

We assume that the system fragments and forms a granular source of many QGP droplets at a time $t_0 (> \tau_0 = 1$ fm/c). The fragmentation may be due to the violent expansion of the system with large fluctuation of initial matter distribution [16] or the rapidly increased bulk viscosity in the QGP near the phase transition [45]. Because of the surface tension of the QGP, the droplet has a spherical geometry in its local frame. We assume that the initial radii r'_0 of the droplets in droplet local frame have a Gaussian distribution with standard deviation a , and the initial droplet centers are distributed within a short cylinder along the beam direction (z direction) with the probabilities [16]

$$\frac{dP_\perp}{2\pi\rho_0 d\rho_0} \propto [1 - \exp(-\rho_0^2/\Delta\mathcal{R}_\perp^2)] \theta(\mathcal{R}_\perp - \rho_0), \quad (23)$$

$$\frac{dP_y}{dy_0} = \theta(y_m - |y_0|), \quad z_0 = t_0 \tanh y_0, \quad (24)$$

where ρ_0 and z_0 are the initial transverse and longitudinal coordinates of the droplet, y_0 is the initial rapidity of the droplet, and \mathcal{R}_\perp and $\Delta\mathcal{R}_\perp$ are the initial transverse radius and shell parameter of the granular source. In our calculations we take $\mathcal{R}_\perp = 6.8$ fm, $\Delta\mathcal{R}_\perp = 3.3$ fm, and $a = 2.3$ fm. The initial temperature of the droplets is taken to be 200 MeV and the quantities y_m and t_0 are taken to be 1.5 and 5.0 fm/c.

The velocity of a droplet depends on its initial central-coordinate (ρ_0, z_0) . Based on Eq. (22) we assume that the velocity of the droplet is given by

$$v_{d\perp} = a_T \left(\frac{\rho_0}{\mathcal{R}_\perp} \right)^{b_T} \sqrt{1 - v_{dz}^2}, \quad v_{dz} = z_0/t_0, \quad (25)$$

where a_T and b_T are the magnitude and exponential power parameters determined by the particle transverse momentum distribution.

The evolution of the system after t_0 is the superposition of all the evolutions of the individual droplets, each of them is described by relativistic hydrodynamics with the equation of state (EOS) of the entropy density [46, 47, 48]. The values of the EOS parameters we used are the transition temperature $T_c = 170$ MeV, the transition temperature width $\Delta T_c = 0.05T_c$, the bag constant $B = 250$ MeV/fm³, and the ratio of the degrees of freedom of the QGP to the hadronic gas $d_Q/d_H = 3.6$.

In order to include the pions emitted directly at hadronization and decayed from resonances later, we let the pions freeze-out (emit out from the source) within a wide temperature region with the probability

$$\begin{aligned} \frac{dP_f}{dT} &\propto f_{\text{dir}} \exp[-(T - T_h)/\Delta T_{\text{dir}}] \\ &+ (1 - f_{\text{dir}}) \exp[-(T - T_h)/\Delta T_{\text{dec}}], \end{aligned} \quad (26)$$

where f_{dir} is a fraction parameter for the direct emission, T_h represents the temperature of complete hadronization, ΔT_{dir} and ΔT_{dec} describe the widths of temperature for the direct and decayed pion emissions.

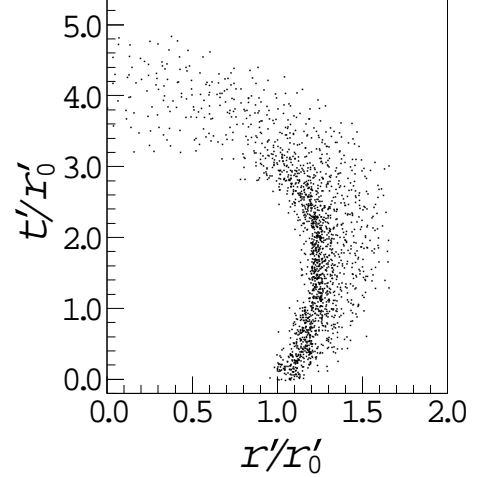


FIG. 3: The space-time distribution of pion-emitting points in the center-of-mass frame of droplet.

Figure 3 shows the space-time distribution of pion-emitting points in the center-of-mass frame of droplet. Considering that most pions are emitted directly from the hadronization configuration and the decayed pions are produced within a larger temperature region, we take the parameters in Eq. (26) to be $f_{\text{dir}} = 0.85$, $\Delta T_{\text{dir}} = 10$ MeV, and $\Delta T_{\text{dec}} = 90$ MeV in our calculations. The complete hadronization temperature T_h is taken to be $0.9T_c$.

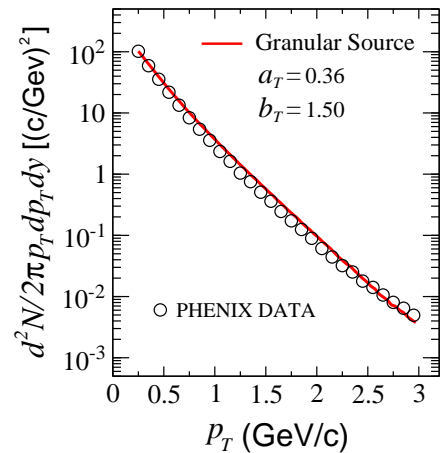


FIG. 4: (Color online) The pion transverse momentum distribution of the granular source and the PHENIX data for $\sqrt{s_{\text{NN}}} = 200$ GeV Au+Au collisions with minimum bias [49].

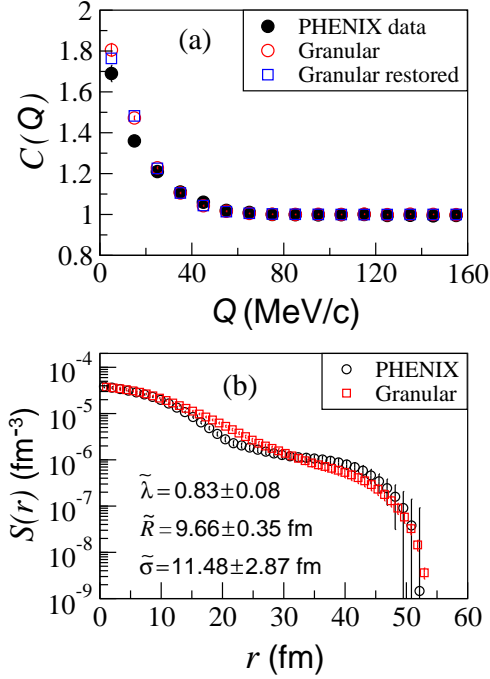


FIG. 5: (Color online) (a) The two-pion correlation functions of the granular source and PHENIX experiment [50]. (b) The imaging results corresponding to the correlation functions in (a).

In Fig. 4, we exhibit the pion transverse momentum distribution of the granular source. By comparing with the experimental data [49], we determine the velocity parameters of the droplet in Eq. (25) as $a_T = 0.36$ and $b_T = 1.50$. In Figure 5 (a) we show the two-pion correlation functions $C(Q)$ of the granular source (open circle) and PHENIX experiment $\sqrt{s_{\text{NN}}} = 200$ GeV Au+Au collisions (solid circle) [50]. In Fig. 5 (b) we show the source functions $S(r)$ corresponding to the correlation functions in Fig. 5 (a). It can be seen that the source function of the granular source exhibits a long tail as the experimental result. The symbols \square in Fig. 5 (a) are for the restored correlation function of the granular source. It is consistent with the original correlation function of the granular source. The difference between the granular and experimental correlation functions at small Q may be arising from the final state interaction and the coherence of pion emission which we have not considered in our granular source model.

IV. SOURCE HBT CHARACTERISTIC QUANTITIES

In this section we examine the three-dimension imaging of the improved granular source with the technique proposed by Danielewicz and Pratt [30, 31]. We will investigate the characteristic quantities $\tilde{\lambda}$, \tilde{R} , and $\tilde{\sigma}$ in

different directions as well as the usual HBT radii R_{out} , R_{side} , and R_{long} for the granular source.

Using a Cartesian harmonic basis $\{\mathcal{A}_{\alpha_1, \dots, \alpha_l}^l(\Omega)\}$ ($l = 0, 1, 2, \dots$; $\alpha_i = x, y$, or z) [30, 31], the three-dimension correlation function $\mathcal{R}(\mathbf{Q}) = C(\mathbf{Q}) - 1$ and source function $S(\mathbf{r})$ in PCMS can be expressed as [10, 30, 31]

$$\mathcal{R}(\mathbf{Q}) = \sum_{l, \alpha_1, \dots, \alpha_l} R_{\alpha_1, \dots, \alpha_l}^l(Q) \mathcal{A}_{\alpha_1, \dots, \alpha_l}^l(\Omega_{\mathbf{Q}}), \quad (27)$$

$$S(\mathbf{r}) = \sum_{l, \alpha_1, \dots, \alpha_l} S_{\alpha_1, \dots, \alpha_l}^l(r) \mathcal{A}_{\alpha_1, \dots, \alpha_l}^l(\Omega_{\mathbf{r}}), \quad (28)$$

where \mathbf{Q} and \mathbf{r} are the relative momentum and coordinate of the pion pair in PCMS, Q and $\Omega_{\mathbf{Q}}$ are the modulus and solid angle of \mathbf{Q} , and r and $\Omega_{\mathbf{r}}$ are the modulus and solid angle of \mathbf{r} . From the Koonin-Pratt formalism [37, 51], the relation of $R_{\alpha_1, \dots, \alpha_l}^l(Q)$ and $S_{\alpha_1, \dots, \alpha_l}^l(r)$ is given by [10, 30, 31]

$$R_{\alpha_1, \dots, \alpha_l}^l(Q) = 4\pi \int dr r^2 \mathcal{K}_l(Q, r) S_{\alpha_1, \dots, \alpha_l}^l(r), \quad (29)$$

where [29, 31]

$$\mathcal{K}_l(Q, r) = \begin{cases} (-1)^{l/2} j_l(Qr), & \text{for even } l, \\ 0, & \text{for odd } l, \end{cases} \quad (30)$$

if neglecting the final state interaction of the pion pair.

From Eq. (27) one can get $R_{\alpha_1, \dots, \alpha_l}^l(Q)$ from the measured three-dimension correlation function $\mathcal{R}(\mathbf{Q})$ [10, 30, 31],

$$R_{\alpha_1, \dots, \alpha_l}^l(Q) = \frac{(2l+1)!!}{l!} \int \frac{d\Omega_{\mathbf{Q}}}{4\pi} \mathcal{A}_{\alpha_1, \dots, \alpha_l}^l(\Omega_{\mathbf{Q}}) \mathcal{R}(\mathbf{Q}). \quad (31)$$

Then, using the one-dimension imaging technique [5, 22, 23] one can get $S_{\alpha_1, \dots, \alpha_l}^l(r)$ by Eq. (29), and finally get the three-dimension source function $S(\mathbf{r})$ with Eq. (28).

In Fig. 6 we show the independent $R_{\alpha_1, \dots, \alpha_l}^l(Q)$ up to $l = 4$ for the granular source. Here $R^0(Q)$ is the correlation function averaged over angles, the index “ $\alpha_i 2$ ”, “ $\alpha_i 4$ ”, and “ $\alpha_i 2 \alpha_j 2$ ” denote “ α_i, α_i ”, “ $\alpha_i, \alpha_i, \alpha_i, \alpha_i$ ”, and “ $\alpha_i, \alpha_i, \alpha_j, \alpha_j$ ”, respectively. Because of source symmetry, the components with odd l are zero. We use x and y denote the directions parallel and perpendicular to the transverse momentum of the pion pair, and let z -axis along the longitudinal (beam) direction. The x , y , and z directions are usually called as “out”, “side”, and “long” directions in HBT interferometry [36, 37].

The source function along the j -axis ($r = r_j$, $j = x, y$, or z) can be expressed as [10, 30, 31]

$$S(r_j) = S^0(r_j) + S_{j2}^2(r_j) + S_{j4}^4(r_j) + \dots, \quad (32)$$

where S^0 is the angle-averaged source function and S_{jl}^l ($l = 2, 4, \dots$) are the l -order modifications for S^0 in the j -direction.

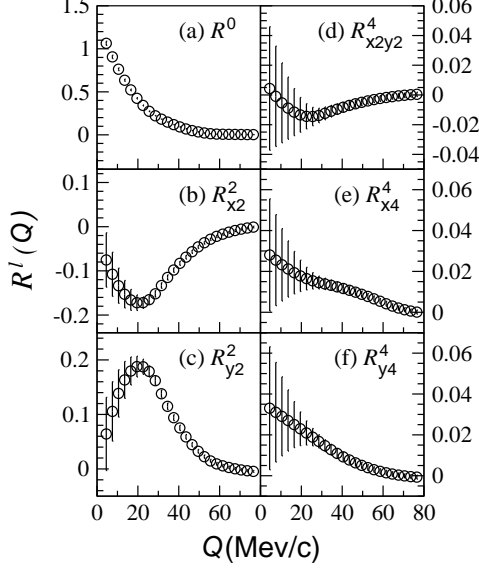


FIG. 6: The independent $R_{\alpha_1, \dots, \alpha_l}^l(Q)$ up to $l = 4$ for the granular source.

In Fig. 7 we show the three-dimension source functions of the granular source for $k_T < 350$ MeV/c and $k_T > 350$ MeV/c, where $k_T = |\mathbf{p}_{1T} + \mathbf{p}_{2T}|/2$ is the transverse momentum of pion pair in the longitudinally co-moving system (LCMS) [4]. One can see that the widths of the source functions in “out” direction are larger than those in “side” direction as observed in experiments [10]. This reflects that the source expansion, which boosts the pair velocity (momentum), leads to different geometries in “out” and “side” directions. For higher k_T , the width of the source function in “out” direction is larger than that for lower k_T . However, in “side” direction the width of the source function are smaller for higher k_T than that for lower k_T . The source function in longitudinal direction has a long tail for the pion pairs with lower k_T for the granular source. It is because that the average longitudinal velocity of pion pairs is larger for smaller k_T . Our model calculations indicate that the average velocity of the pair in longitudinal direction is about 0.43 for $k_T < 350$ MeV/c and 0.35 for $k_T > 350$ MeV/c. In Fig. 8 we show the angle-averaged source functions $S^0(r)$ and the “second-order” and “fourth-order” source functions $S^2(r)$ and $S^4(r)$ in “out”, “side”, and “long” directions for $k_T < 350$ MeV/c and $k_T > 350$ MeV/c for the granular source. It can be seen that the one-dimension imaging S^0 of the granular source exhibits a “two-tiered” structure [12]. The fourth-order source functions are almost zero exception for that at small r .

In order to examine the three-dimension source functions quantitatively, we introduce the moments of r_i for

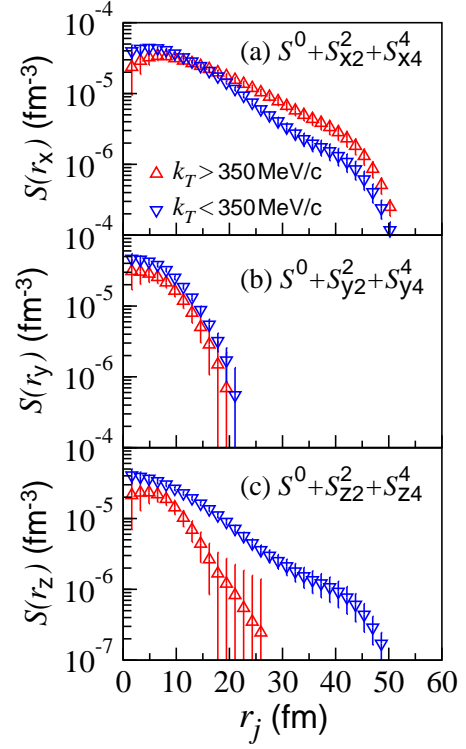


FIG. 7: (Color online) The three-dimension source functions of the granular source for $k_T < 350$ MeV/c and $k_T > 350$ MeV/c. $r_j = r_x, r_y$, or r_z .

the “ i -component” of the source function,

$$\langle r_i^n \rangle = \frac{\int_0^\infty dr_i r_i^n S(r_i)}{\int_0^\infty dr_i S(r_i)}, \quad n = 1, 2, \dots, \quad (33)$$

and define the normalized first-order moment and deviation as

$$\tilde{R}_i \equiv \frac{\sqrt{\pi}}{2} \langle r_i \rangle \quad (34)$$

and

$$\tilde{\sigma}_i \equiv \sigma_i / \sqrt{2 - 4/\pi}, \quad (35)$$

which are normalized to the Gaussian radius R_{ga} for a one-dimension Gaussian source [$S(r_i) \sim \exp(r_i^2/4R_{\text{ga}}^2)$].

In Fig. 9 (a), (b), and (c) we exhibit the normalized first-order moments (symbols \triangle) of the granular source as functions of k_T in “out”, “side”, and “long” directions, respectively. \tilde{R}_x increases and \tilde{R}_y decreases with k_T as expected. Because the average longitudinal velocity of the pairs with larger k_T is smaller, \tilde{R}_z decreases with k_T . Figure 9 (d) gives the results of $\tilde{\lambda}$ calculated with the angle-averaged source function $S^0(r)$ in Eq. (14) for the granular source. The results of $\tilde{\lambda}$ decrease with k_T . In Fig. 9 (e) we show the ratios $\tilde{\sigma}_j/\tilde{R}_j$ ($j = x, y, z$) for the granular source. The large value of $\tilde{\sigma}_z/\tilde{R}_z$ at small k_T indicates that the source function have a serious deviation

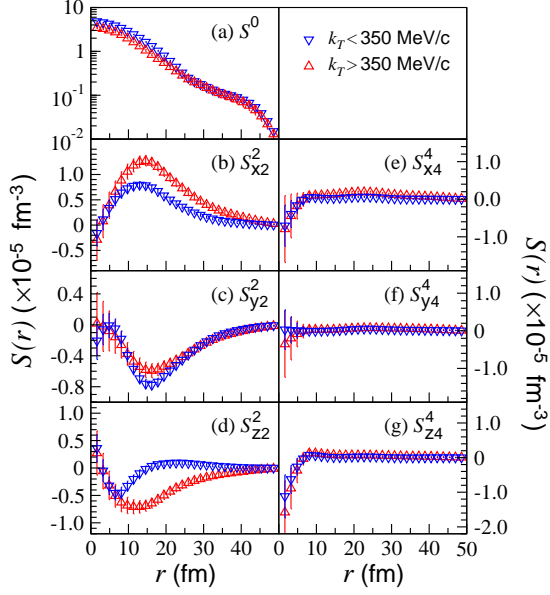


FIG. 8: (Color online) The zero-order, second-order, and fourth-order source functions $S^0(r)$, $S^2(r)$, and $S^4(r)$ in “out”, “side”, and “long” directions for $k_T < 350$ MeV/c and $k_T > 350$ MeV/c for the granular source.

from that of a Gaussian source in longitudinal direction. However, in “side” direction the ratios are almost unit.

The first-order moments \tilde{R}_x , \tilde{R}_y , and \tilde{R}_z describe the average separations of the source in PCMS. In LCMS the pair has a transverse velocity $v_T (= k_T / [(E_1 + E_2)/2])$. The spatial separation in LCMS in “out” direction is smaller than \tilde{R}_x by the Lorentz contraction factor $\gamma_T^{-1} = \sqrt{1 - v_T^2}$ [37]. In Fig. 9 (a), the symbols ∇ denote the results of $\gamma_T^{-1} \tilde{R}_x$. One can see that $\gamma_T^{-1} \tilde{R}_x$ decrease with k_T as that of the HBT radius R_{out} in LCMS [1, 2, 3, 4]. For comparison, in Fig. 9 (f) – (j) we exhibit the HBT radii and chaotic parameter for the granular source fitted with

$$C(q_{\text{out}}, q_{\text{side}}, q_{\text{long}}) = 1 + \lambda e^{-q_{\text{out}}^2 R_{\text{out}}^2 - q_{\text{side}}^2 R_{\text{side}}^2 - q_{\text{long}}^2 R_{\text{long}}^2}, \quad (36)$$

in LCMS and the experimental HBT results of PHENIX [34] and STAR [35] for $\sqrt{s_{\text{NN}}} = 200$ GeV Au+Au collisions. One can see that the HBT radii as functions of k_T for the granular source agree with the experimental results. Also, the separations $\gamma_T^{-1} \tilde{R}_x$, \tilde{R}_y , and \tilde{R}_z as functions of k_T agree with those of the corresponding HBT radii R_{out} , R_{side} , and R_{long} . At lower k_T the values of the chaotic parameter λ are smaller than those of $\tilde{\lambda}$ obtained by imaging analysis, and both the values of λ and $\tilde{\lambda}$ of the granular source are larger than the experimental λ results. The results of $R_{\text{out}}/R_{\text{side}}$ for the granular source are consistent with the experimental data. The granular source model reproduce the main characteristics of the source functions as well as HBT radii of RHIC experimental measurements [10, 34, 35].

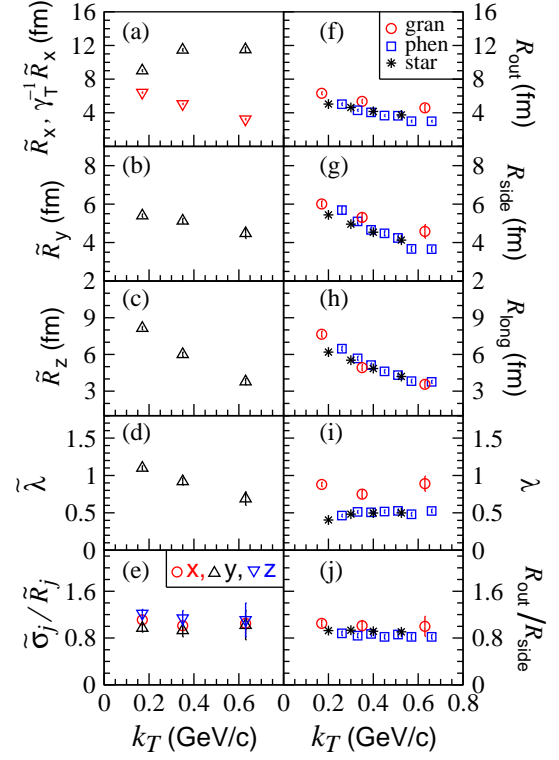


FIG. 9: (Color online) (a)–(e) The characteristic quantities of three-dimension imaging as functions of k_T for the granular source. (f)–(j) The HBT Gaussian fitted results for the granular source compared with the results of RHIC experiments [34, 35].

V. SUMMARY AND CONCLUSION

Imaging analysis is a model-independent technique [5, 22, 23]. With the source functions obtained by the three-dimension imaging technique [30, 31], one can calculate numerically the first-, second-, and even higher-order moments of the spatial separation r in different directions. In principle, the detailed information about the source geometry, coherence, and dynamics can be extracted by analyzing these moments.

In this paper we examine the spatial and coherent information of pion-emitting source extracted by usual HBT Gaussian fit and imaging analysis in relativistic heavy ion collisions. The usual HBT results of the Gaussian fit are model-dependent. They are inappropriate for describing the characteristics of the sources with non-Gaussian distributions, such as the sources with granular and core-halo structures. However, the zero- and first-order moments as well as the deviation of two-pion source separation $(\tilde{\lambda}, \tilde{R}, \tilde{\sigma})$ obtained by imaging analysis can provide better descriptions for the source coherent and spatial characteristics. They are model-independent characteristic quantities of the particle-emitting sources.

Based on an improved granular source model we inves-

tigate the characteristic quantities of the pion-emitting source produced in relativistic heavy ion collisions. We find that the granular source model of QGP droplets can reproduce the main characteristics of the experimental two-pion correlation functions and source functions in $\sqrt{s_{\text{NN}}} = 200$ GeV Au+Au collisions [10, 34, 35]. In the transverse directions of the collisions, the width of the source function in “out” direction is larger than that in “side” direction. Correspondingly, the value of the first-order moment \tilde{R}_x is larger than that of \tilde{R}_y . The dependence of \tilde{R}_j on the transverse momentum of the pair k_T exhibits different in “out” and “side” directions. \tilde{R}_x increases but \tilde{R}_y decreases with k_T increase. In the longitudinal direction, the source function for small k_T has a long tail, which is much different from the Gaussian source function. Correspondingly, the value of $\tilde{\sigma}_z/\tilde{R}_z$ is large at small k_T . We find that \tilde{R}_z decrease rapidly with k_T increase. After taking into account the Lorentz contraction in “out” direction, all the quantities $\gamma_T^{-1}\tilde{R}_x$, \tilde{R}_y , and \tilde{R}_z decrease with k_T increase. These transverse-momentum dependences for the granular source are consistent with those of the usual HBT Gaussian fit results of R_{out} , R_{side} , and R_{long} . They are also consistent with

the results of RHIC experiments [34, 35].

From our model results we notice that both the values of $\tilde{\lambda}$ and λ , obtained by the imaging analysis and HBT Gaussian fit, are larger than the experimental results of λ [34, 35]. Except for the source coherence, there are other elements which may affect the results of $\tilde{\lambda}$ and λ , such as the Coulomb interaction of the final-state particles and source dynamics [1, 2, 3, 4, 52]. Investigating the effects of these elements on $\tilde{\lambda}$ and λ for the granular source will be an interesting issue. On the other hand, because imaging analysis is performed in PCMS the temporal information of the particle emission is hidden [5, 52]. Further investigation on how to extract the temporal information of the source by analyzing the spatial moments in different directions and their k_T dependences will be also of interest.

Acknowledgments

This research was supported by the National Natural Science Foundation of China under Contract No. 10775024.

-
- [1] C. Y. Wong, *Introduction to High-Energy Heavy-Ion Collisions* (World Scientific, Singapore, 1994), Chap. 17.
 - [2] U. A. Wiedemann and U. Heinz, Phys. Rept. **319**, 145 (1999).
 - [3] R. M. Weiner, Phys. Rept. **327**, 249 (2000).
 - [4] M. A. Lisa, S. Pratt, R. Soltz, U. Wiedemann, Ann. Rev. Nucl. Part. Sci. **55**, 357 (2005); nucl-ex/0505014.
 - [5] D. A. Brown and P. Danielewicz, Phys. Rev. C **64**, 014902 (2001).
 - [6] P. Chung, A. Taranenko, R. Lacey, W. Holzmann, J. Alexander, M. Issah, Nucl. Phys. A **749**, 275c (2005).
 - [7] S. S. Adler *et al.*, (PHENIX Collaboration), Phys. Rev. Lett. **98**, 132301 (2007).
 - [8] P. Chung and P. Danielewicz (for the NA49 Collaboration), J. Phys. G **34**, S1109 (2007).
 - [9] P. Chung (for the PHENIX Collaboration), J. Phys. G **35**, 044034 (2008).
 - [10] S. Afanasiev *et al.*, (PHENIX Collaboration), Phys. Rev. Lett. **100**, 232301 (2008).
 - [11] Roy A. Lacey (for the PHENIX Collaboration), J. Phys. G **35**, 104139 (2008).
 - [12] Z. T. Yang, W. N. Zhang, L. Huo, and J. B. Zhang, J. Phys. G **36**, 015113 (2009).
 - [13] Zi-wei Lin, C. M. Ko, and Subrata Pal, Phys. Rev. Lett. **89**, 152301 (2002).
 - [14] Zi-wei Lin and C. M. Ko, J. Phys. G **30**, S263 (2004).
 - [15] T. Csörgő, S. Hegyi, and W. A. Zajc, Eur. Phys. J. C **36**, 67 (2004).
 - [16] W. N. Zhang, Y. Y. Ren, and C. Y. Wong, Phys. Rev. C **74**, 024908 (2006).
 - [17] Y. Y. Ren, W. N. Zhang, and J. L. Liu, Phys. Lett. B **669**, 317 (2008).
 - [18] S. Nickerson, T. Csörgő, and D. Kiang, Phys. Rev. C **57**, 3251 (1998).
 - [19] Ulrich Heinz and Barbara V. Jacak, Ann. Rev. Nucl. Part. Sci. **49**, 529 (1999); nucl-th/9902020.
 - [20] D. Hardtke and S. A. Voloshin, Phys. Rev. C **61**, 024905 (2000).
 - [21] E. Frodermann, U. Heinz and M. A. Lisa, Phys. Rev. C **73**, 044908 (2006).
 - [22] D. A. Brown and P. Danielewicz, Phys. Lett. B **398**, 252 (1997).
 - [23] D. A. Brown and P. Danielewicz, Phys. Rev. C **57**, 2474 (1998).
 - [24] D. A. Brown, S. Y. Panitkin, and G. F. Bertsch, Phys. Rev. C **62**, 014904 (2000).
 - [25] S. Y. Panitkin *et al.*, (E895 Collaboration), Phys. Rev. Lett. **87**, 112304 (2001).
 - [26] G. Verde, D. A. Brown, P. Danielewicz, C. K. Gelbke, W. G. Lynch, and M. B. Tsang, Phys. Rev. C **65**, 054609 (2002).
 - [27] P. Chung *et al.*, (E895 Collaboration), Phys. Rev. Lett. **91**, 162301 (2003).
 - [28] P. Danielewicz, D. A. Brown, M. Heffner, S. Pratt, and R. Soltz, Acta Phys. Hung. A **22**, 253 (2005); nucl-th/0407022.
 - [29] D. A. Brown, A. Enokizono, M. Heffner, R. Soltz, P. Danielewicz, and S. Pratt, Phys. Rev. C **72**, 054902 (2005).
 - [30] P. Danielewicz and S. Pratt, Phys. Lett. B **618**, 60 (2005).
 - [31] Pawel Danielewicz and Scott Pratt, Phys. Rev. C **75**, 034907 (2007).
 - [32] C. Adler *et al.* (STAR Collaboration), Phys. Rev. Lett. **87**, 082301 (2001).
 - [33] K. Adcox *et al.* (PHENIX Collaboration), Phys. Rev.

- Lett. **88**, 192302 (2002).
- [34] S. S. Adler *et al.* (PHENIX Collaboration), Phys. Rev. Lett. **93**, 152302 (2004).
 - [35] J. Adams *et al.* (STAR Collaboration), Phys. Rev. C **71**, 044906 (2005).
 - [36] G. Bertsch, M. Gong, M. Tohyama, Phys. Rev. C **37**, 1896 (1988); G. Bertsch, Nucl. Phys. A **498**, 173c (1989).
 - [37] S. Pratt, T. Csörgő and J. Zimányi, Phys. Rev. C **42**, 2646 (1990).
 - [38] W. N. Zhang, M. J. Efaaf, and C. Y. Wong, Phys. Rev. C **70**, 024903 (2004).
 - [39] S. Pratt, P. J. Siemens, and A. P. Vischer, Phys. Rev. Lett. **68** 1109, (1992).
 - [40] W. N. Zhang, Y. M. Liu, L. Huo, Y. Z. Jiang, D. Keane, and S. Y. Fung, Phys. Rev. C **51**, 922 (1995).
 - [41] T. Csörgő, B. Lörstad, and J. Zimányi, Z. Phys. C **71**, 491 (1996).
 - [42] Z. T. Yang, Y. Y. Ren, C. C. Gao, and W. N. Zhang, Nucl. Phys. Rev. **26** (2009) (in Chinese).
 - [43] J. D. Bjorken, Phys. Rev. D **27**, 140 (1983).
 - [44] G. Baym, B. L. Friman, J. P. Blaizot, M. Soyeur, and W. Czyz, Nucl. Phys. **A407**, 541 (1983).
 - [45] G. Torrieri, B. Tomášik, I. Mishustin, Phys. Rev. C **77**, 034903 (2008).
 - [46] D. H. Rischke and M. Gyulassy, Nucl. Phys. **A608**, 479 (1996).
 - [47] J. P. Blaizot J. Y. Ollitrault, Phys. Rev. D **36**, 916 (1987).
 - [48] E. Laermann, Nucl. Phys. **A610**, 1 (1996).
 - [49] S. S. Adler *et al.* (PHENIX Collaboration), Phys. Rev. C **69**, 034909 (2004).
 - [50] S. S. Adler *et al.* (PHENIX Collaboration), nucl-ex/0401003.
 - [51] S. E. Koonin, Phys. Lett. B **70**, 43 (1977).
 - [52] S. Pratt, Phys. Rev. D **33** 72, (1986).